

Decoding Silent Speech Cues From Muscular Biopotential Signals for Efficient Human-Robot Collaborations

Penghao Dong, Sibo Tian, Si Chen, Yizong Li, Su Li, Minghui Zheng, and Shanshan Yao*

Silent speech interfaces offer an alternative and efficient communication modality for individuals with voice disorders and when the vocalized speech communication is compromised by noisy environments. Despite the recent progress in developing silent speech interfaces, these systems face several challenges that prevent their wide acceptance, such as bulkiness, obtrusiveness, and immobility. Herein, the material optimization, structural design, deep learning algorithm, and system integration of mechanically and visually unobtrusive silent speech interfaces are presented that can realize both speaker identification and speech content identification. Conformal, transparent, and self-adhesive electromyography electrode arrays are designed for capturing speech-relevant muscle activities. Temporal convolutional networks are employed for recognizing speakers and converting sensing signals into spoken content. The resulting silent speech interfaces achieve a 97.5% speaker classification accuracy and 91.5% keyword classification accuracy using four electrodes. The speech interface is further integrated with an optical hand-tracking system and a robotic manipulator for human-robot collaboration in both assembly and disassembly processes. The integrated system achieves the control of the robot manipulator by silent speech and facilitates the hand-over process by hand motion trajectory detection. The developed framework enables natural robot control in noisy environments and lays the ground for collaborative human-robot tasks involving multiple human operators.

1. Introduction

The silent speech interface (SSI) converts non-acoustically acquired cues to speech. Such interfaces have been pursued to help people with voice disorders caused by diseases, laryngectomy, accidents, vocal abuse, or aging.^[1-3] Compared with voice-, touch-, and gesture-based input modalities, silent speech input is

found to be more desirable due to the enhanced privacy, hands-free accessibility, less specialized training, high efficiency (e.g., voice interaction is 3x faster than typing), and for being highly informative.^[4-6] For industrial applications, the system is particularly useful when voice-based speech signals are compromised by noisy environments. These characteristics have made SSI a great alternative to vocalized speech recognition for interaction with robots, machines, and smart devices.

Speech recognition has been previously reported as a method for issuing commands to robots in human-robot collaboration (HRC).^[7-12] Unlike traditional industrial robots that follow preprogrammed routines, collaborative robots share the same workspaces with humans,^[13-15] and dynamically adjust tasks to assist human operators throughout the entire manufacturing process.^[16] For instance, robots can assist human operators by handling components and delivering them upon receiving commands during assembly tasks,^[13,17] allowing human operators to focus on higher-level decision-making. This adaptability of

robots necessitates an understanding of human operators' commands and motions, which enables robots to anticipate human intentions and adjust their behavior accordingly. However, speech recognition in manufacturing scenarios faces several challenges: Noises from machines, workers, and other sources negatively affect the accuracy of speech recognition, consequently reducing the overall performance of HRC. In addition, individuals with voice disorders are unable to generate audible speech commands for robot control. These problems can be mitigated by seamlessly integrating SSI into HRC for more efficient robot control.

The SSI should exhibit good recognition accuracy, portability, wearing comfort, noninvasiveness, and unobtrusiveness on the skin surface. However, existing SSIs can only meet some of these criteria, restricting their wide acceptance and deployment. As summarized in Table S1 (Supporting Information), SSIs based on different methods can be categorized into two primary groups: Contactless approaches and contact-based approaches. Contactless methods mainly utilize vision cues, ultrasound imaging, or wireless signals to capture speech-induced

P. Dong, S. Chen, Y. Li, S. Li, S. Yao
Department of Mechanical Engineering
Stony Brook University
Stony Brook, NY 11794, USA
E-mail: shanshan.yao@stonybrook.edu

S. Tian, M. Zheng
Department of Mechanical Engineering
Texas A&M University
College Station, TX 77843, USA

 The ORCID identification number(s) for the author(s) of this article can be found under <https://doi.org/10.1002/admt.202400990>

DOI: 10.1002/admt.202400990

movement profiles of different articulators.^[18–25] For instance, vision-based methods are effective in tracking lip and neck movements for silent speech recognition but require constant line-of-sight without occlusion.^[18–21] The accuracy of speech recognition can be affected by the angle of capturing cameras, lighting conditions, and the user's daily motions. Setting up a camera can be inconvenient, socially inappropriate, and has the concern of capturing sensitive information.^[1] In general, contactless methods are not hands-free, relying on external devices, and the accuracy can be affected by environmental interferences and alignment issues.

Alternatively, for contact-based methods, face-worn or implantable sensors are employed to capture biopotentials from the brain and muscle, or movement of articulators involved in speech. Implantable sensors have been explored to detect tongue movements using attached magnets,^[26,27] to interpret signals from the speech motor cortex,^[28] or to measure brain signals on the cortical surface using Electrocorticography (ECOG).^[29–31] These techniques are invasive and often require surgical procedures to implant devices. As less invasive methods, a variety of face-worn sensors are exploited for silent speech recognition. For instance, electroencephalogram (EEG) helmets worn around the head,^[32,33] inertial sensors placed on the temporomandibular joint or the neck,^[4,34,35] magnets or electromagnetic devices placed inside or around the mouth,^[36–38] earphones placed in the ear canal,^[39] and RFID tags mounted around the mouth^[40] have been utilized to capture bio-signals and movement patterns. Among these efforts, the flexible RFID tags rely on expensive and bulky commodity RFID readers. The system is also vulnerable to the tags' relative location to the reader and the dynamic radio environment. Other methods typically implement bulky or rigid devices that may constrain natural movements associated with speech generation. Stretchable epidermal strain^[41,42] and electromyography (EMG) sensors^[43,44] that can better adapt to skin movements are emerging for speech recognition. However, the recognition accuracy using the strain sensor requires further improvement. The reported stretchable EMG electrodes employ metallic films as conductive elements, which are highly visible on the skin surface and lack inherent adhesion. Our previous work^[45] employed metallic nanowires-enabled electrodes for silent speech recognition, which necessitates eight electrodes placed on the skin surface that are not fully transparent. Developed electrodes can achieve conformal contact^[46–48] with the free-form human skin surface for good signal quality but they were not integrated into one patch. It is challenging for repetitive removal and reattachment of the electrodes to the same location. EMG signals are however very sensitive to electrode locations. Other reported EMG electrodes are mainly built upon conductive polymers, carbon-based nanomaterials, and metallic materials.^[49] These materials are integrated with structural designs such as serpentine structures^[50] and fractal patterns^[51] to maintain electrode performance on deformable surfaces such as the human skin. A primary challenge associated with most reported electrodes for SSIs is their lack of transparency, making them unsuitable for aesthetically sensitive areas (e.g., the face), particularly for long-term use. Various manufacturing methods, including electrohydrodynamic jet printing,^[52] laser patterning,^[53] and sputtering,^[54] have been employed to fabricate these electrodes for deformable 3D freeform surfaces. To

promote the wide acceptance of SSI systems for daily use, low-cost, scalable, and reliable manufacturing methods are in demand for preparing electrode arrays on the skin surface. On the other hand, standalone stretchable devices, typically consisting of sensors, microcontrollers, data storage, wireless communication modules, and portable power sources have been developed for monitoring various physiological signals and body motions.^[55,56] Such platforms enable fully stretchable and conformable skin interfaces that promote a paradigm shift in healthcare, activity tracking, and human-computer interfaces. The SSIs will also benefit from further development of standalone stretchable devices that integrate sensing electrodes, data collection, machine learning algorithms, and data transmission components in one stretchable platform.

In this work, we present an unobtrusive SSI enabled by a transparent and integrated EMG electrode array as well as a framework for incorporating SSI into HRC (Figure 1a–g). Instead of relying on traditional voice-based speech recognition, this work highlights an SSI that collects lip movements wirelessly and decodes the signals into commands for robot control. A low-cost, self-adhesive, fully transparent, and conformal electrode array is designed and integrated for detecting speech cues from the surface EMG signals of the facial skin. With a wireless data acquisition interface and a deep learning algorithm for speech recognition, the entire silent speech system is portable, unobtrusive, and effective in interpreting silent speech cues for robot control. The utilized temporal convolutional networks (TCN) model ensures high accuracies for speaker classification and speech content classification in real-time. A motion capture system is employed to detect the hand motion of the human operator for triggering the hand-over process between the robot and the human operator. The potentials of the developed framework for HRC are demonstrated in three human-robot collaborative tasks, including a collaborative robot assisting a human operator in both assembly and disassembly tasks, and a collaborative robot working alongside two human operators in disassembly tasks. The main contributions of this work include (1) the development of an adhesive, integrated, mechanically and visually imperceptible EMG sensing array for tracking subtle speech-relevant muscle activities, (2) the exploration of TCN model for both speaker identification and speech content identification, which allows multiple human operators to work alongside one robot, and (3) the design of an efficient HRC framework comprising SSI and hand motion detection that can engage people with voice disorders and remain robust in a noisy environment.

2. Experimental Section

2.1. Fabrication and Characterizations of the EMG Electrode Array

The transparent EMG electrode array comprises the top insulating layer, middle conducting layer, and bottom substrate layer, along with a flexible cable connecting to the data acquisition circuit board (Figures 1b, and 2a–f). The middle conducting layer consists of sensing electrodes and their interconnects. This was enabled by an optimized mixture of sodium chloride (NaCl), waterborne polyurethane (WPU), ethylene glycol (EG), and deionized (DI) water, where NaCl provides ionic conductive pathways

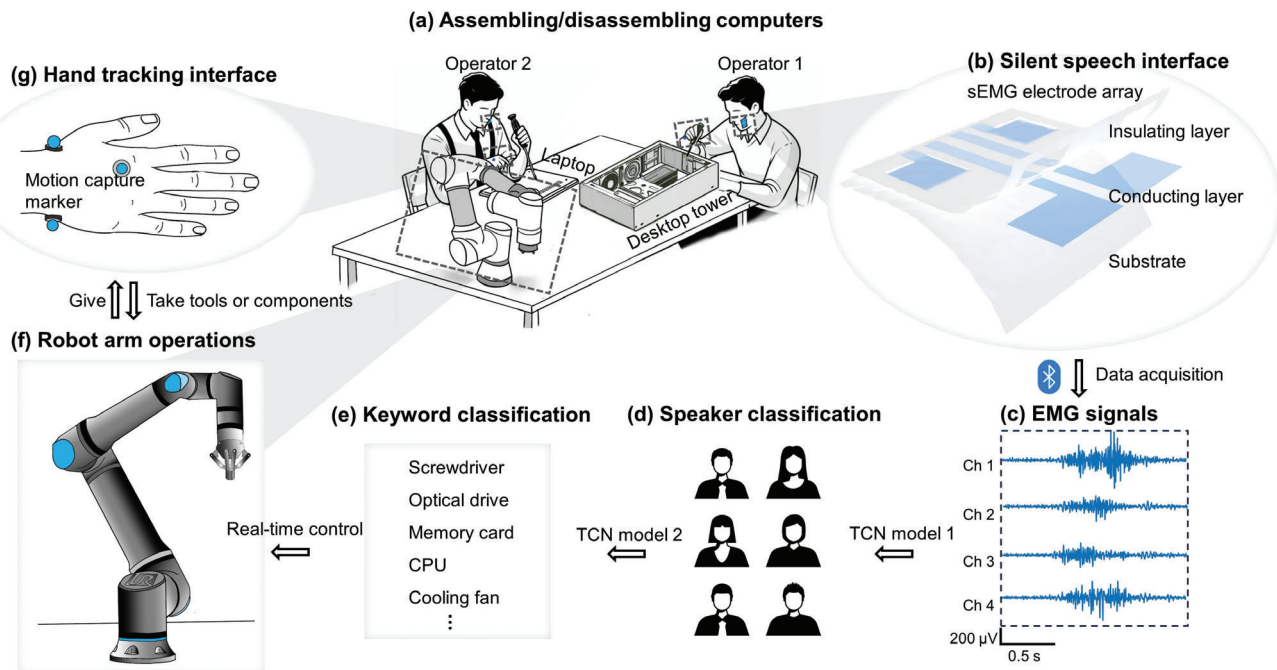


Figure 1. Overview of the silent speech interface enabled human-robot collaborations. a) The collaborative working scenario between humans and robots. b) The structure of the EMG electrode array for robot control via silent speech recognition. c) Example of the collected four-channel EMG signals from the electrode array. d) Speaker classifications using TCN model 1. e) Keyword classifications using TCN model 2. f) The robot manipulator operates by interacting with human hands. g) Hand tracking using motion capture markers placed on the hand.

for biopotential sensing, WPU serves as the polymer matrix, and EG/DI water as the solvent for NaCl. WPU exhibits excellent biocompatibility, skin-like stretchability,^[57] and good adhesion to the skin surface when containing liquids. These characteristics make WPU an excellent choice as the polymer matrix for biopotential electrodes. NaCl can form transparent ionic liquids when dissolved in DI water and EG, while maintaining excellent biocompatibility to human skin.^[58] The addition of EG into DI water retards the dehydration of the ion gel due to the evaporation of DI water. Compared to the evaporation rate of approximately 0.26 mg min^{-1} at room temperature for DI water, a much lower evaporation rate of 0.1 mg min^{-1} was obtained from the mixture of EG and DI water with a weight ratio of 5:1.^[59] In addition, a mixture of EG and DI water was also found to improve the dissolution of NaCl compared with EG alone as the solvent, owing to the fact that the solubility of NaCl in DI water was five times than in EG.^[60] Additionally, encapsulating the ionic liquid into the WPU polymer matrix further reduces the evaporation rate due to the decreased vapor pressure and the formation of a surface film.^[61,62] The top encapsulation layer, based on the insulating Ecoflex Gel, covers the conducting layer except for the sensing electrodes. It provides adhesion to the skin surface and more importantly, electrically isolates the interconnects from the skin surface. This ensures that only sensing electrodes can electrically contact the skin and collect EMG signals, preventing undesired electrical noises generated from interconnects. The bottom substrate layer was made from highly stretchable polydimethylsiloxane (PDMS), which provides structural support to the electrode array. Compared to other biopotential electrodes based on conventional non-stretchable metallic materials,^[43,44,63]

PEDOT:PSS,^[57] carbon materials,^[64] or metallic nanowires,^[50] the fabricated ionically conductive electrode offers several advantages, including increased transparency without sacrificing conductivity, mechanical compliance, adhesion to the skin surface, low cost, and ease of handling. These merits were essential for accurate biopotential sensing and good user acceptance during long-term applications.

The fabrication process of the electrode array was illustrated in Figure 2. Briefly, EG (Sigma-Aldrich), DI water, and NaCl (Sigma-Aldrich) were mixed in a 10:2:1 weight ratio to form a solution. The solution was then added to WPU (UD-410, Bond Polymers) at a weight ratio of 5 to 2 and mixed thoroughly to get the mixture for the conducting layer (Figure 2a). Mixture of 1.5 g was drop-cast onto a glass substrate that was coated with a lower surface energy liner (Figure 2b). The mixture was cured at room temperature for 12 hours. Too short curing time leaves residual liquid (water and EG) on the surface of the ionic conducting layer, leading to delamination between the PDMS and the ionic conducting layer. Then the resulting film was patterned into a desired shape to form the sensing electrodes and interconnects (Figure 2c). To create the substrate layer, 0.5 g PDMS (Sylgard 184, Dow) with the base to curing agent weight ratio of 15:1, was drop-cast and cured at 40 °C for 12 hours (Figure 2d). The structure was flipped (Figure 2e) and a thin layer of Ecoflex Gel (Smooth-On) was coated on the top of the interconnect region. The insulating encapsulation layer was cured at room temperature for 2 hours (Figure 2f). A flexible cable was then connected to the electrode array with the assistance of the silver paste (120-07, Creative Materials). The detailed dimensions of the electrode array were shown in Figure S1 (Supporting Information).

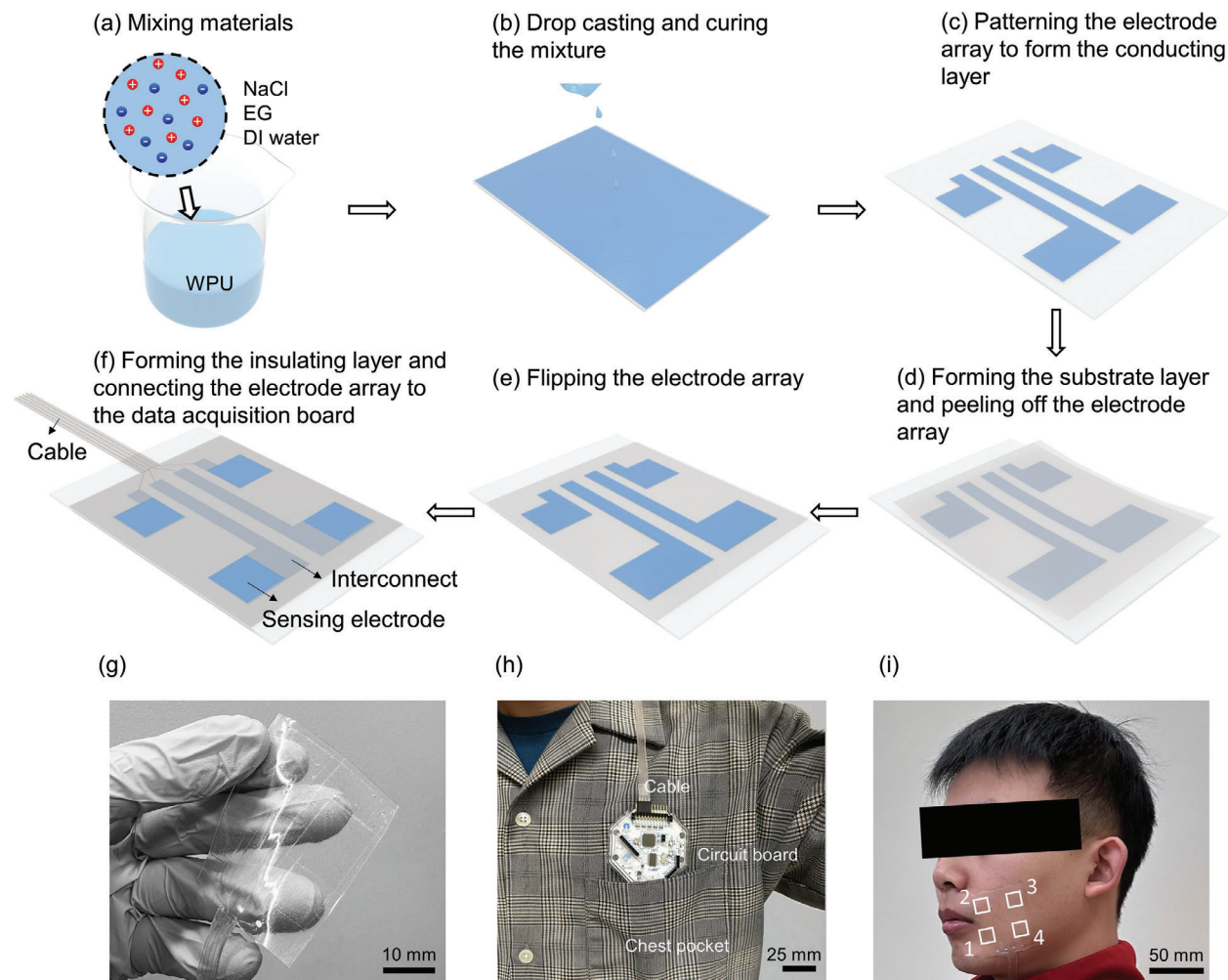


Figure 2. Schematic illustrations of the transparent EMG electrode array. a)–f) Fabrication processes of the EMG electrode array. g) Photograph of the fabricated electrode array. h) The circuit board for EMG data acquisition, which can be put into the chest pocket. The length of the cable can be adjusted to allow the board to be placed in other locations. i) An individual wearing the EMG electrode array on the face with the data acquisition board placed in the chest pocket.

The electrode array (Figure 2g) was attached to the facial skin and linked to a portable Bluetooth biosensing board (OpenBCI Cyton) (Figure 2h; Figure S2, Supporting Information). The detailed components and circuit design of this board were shown in the OpenBCI Documentation.^[65] Following the hardware setup tutorial provided by OpenBCI^[66] and code sample from the open-source BrainFlow,^[67] four-channel EMG signals were collected by using the electrode array as positive sensing electrodes. The exact position of the sensing electrode was shown in Figure 2i and further explained in Section 3.2. Meanwhile, the ground and negative sensing electrodes were attached to the collarbone where muscle activities were minimized.^[45] The signals were collected at a frequency of 250 Hz. Subsequent signal processing involved the application of a bandpass filter with cutoff frequencies set at 20 to 125 Hz and notch filters at 50 and 60 Hz. The lower cutoff frequency at 20 Hz effectively reduces non-speech motion artifacts, which were predominantly present at lower frequencies. The higher cutoff frequency at 125 Hz was determined based on the theoretical consideration

that the maximum cutoff frequency should be half of the sampling frequency.^[68] The notch filter serves to reduce power line interferences.

The electrical, optical, mechanical properties were then evaluated as well as the EMG sensing performance of the fabricated electrode. In specific, one pair of developed electrodes and one pair of commercial electrodes (Kendall, H124SG) were attached to the forearm skin at a distance of 8 cm to compare their electrode-skin impedance using an impedance analyzer (E4990A, Keysight). The EMG signals were collected from both developed electrodes and commercial electrodes for comparing their signal-to-noise ratios (SNRs) during EMG sensing. The transmittance of the electrode was measured by UV-vis Spectroscopy (Genesys 30, Thermal Scientific) across 380 nm to 700 nm visible wavelengths.^[69] The stress-strain curve was measured using the universal mechanical testing system (858 Mini Bionix II, MTS) at a speed of 1 mm min⁻¹. Using the same equipment, the adhesion force of the conducting layer was tested. Rectangular samples were first attached to the glass slide and a skin

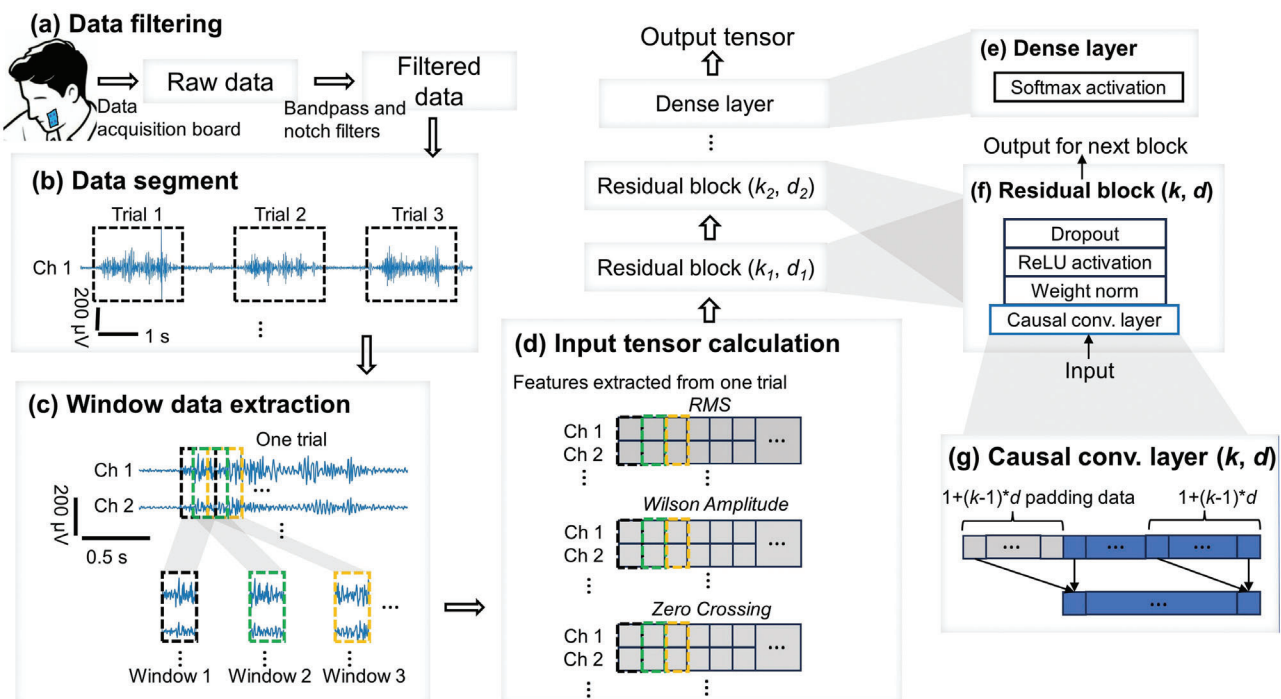


Figure 3. Flow chart showing the signal processing of EMG signals for silent speech recognition: a) data filtering, b) data segment, c) windows data extraction, d) input tensor calculation, and e–g) TCN structure settings.

replica made from Skin Tite (Smooth-On) horizontally. The samples were then subjected to a perpendicular detaching force at a speed of 1 mm min^{-1} . The adhesion force was calculated from the maximum stable force divided by the sample width.^[57] The electrode's stability was evaluated under varying conditions. For testing the stability at different temperatures, a thermoelectric cooler (TEC1-12706, MikroElektronika) was employed to control the local temperature around the skin where the electrode was attached. For assessing stability under different relative humidity levels, a humidifier/dehumidifier air filtration system (HD012, DINZ) and a humidity meter (PT6508, Protmex) were utilized to control and measure the surrounding humidity. Additionally, EMG signals were collected under skin deformations and motion artifacts. EMG signals were collected from different samples to assess sample-to-sample variations and were recorded for five consecutive days to evaluate the long-term stability. An electrochemical impedance spectroscopy (EIS) experiment was conducted to test the ionic conductivity of the electrode. Following the EIS measurement process for ionic materials,^[70] AC signals at frequencies ranging from 0.1 Hz to 7 MHz were applied to the developed ionic materials by a potentiostat (VSP-300, BioLogic) to acquire the Nyquist plot for calculating the ionic conductivity.

2.2. Silent Speech Recognition by TCN Model

Silent speech recognition was performed to decode acquired speech-relevant EMG signals into spoken words. The process consists of two tasks: speaker classification and keyword classification. Both tasks were accomplished by the architecture introduced in **Figure 3**. The EMG raw data was collected from the

EMG electrode array attached to the facial skin (Figure 3a). After a signal filtering process, the data were ready for the data segment (Figure 3b). The data segment served the purpose of extracting silent speech signal trials into the individual segment that lasts two seconds. The data segment algorithm included a global search, a skip function, and a local search (Figure S3, Supporting Information). The global search identified data points exceeding a specified threshold (e.g., $60 \mu\text{V}$), indicating the presence of a nearby silent speech signal trial (Figure S3a, Supporting Information). The skip function then bypassed several data points (e.g., 2.5 seconds of data) to prevent multiple detections within one trial. This process was repeated until the end of the signal. Around each located data point, the local search subsequently identified signal pieces by locating the largest absolute value of the sum of the data point amplitudes (Figure S3b,c, Supporting Information). The top 50 signal pieces having the largest sum of the data point amplitudes were the final extracted trials since each word was repeated 50 times by one individual.

The subsequent step was the execution of window data extraction (Figure 3c). Given that each word comprises multiple syllables and different syllables exhibit distinct signal patterns, it was imperative to segment the extracted signal trial into smaller fragments to enhance classification performance. This method for data extraction of EMG signals was advantageous to the prior work.^[45] As a result, fewer sensing electrodes were required in this work but the classification accuracy was not affected. Figure 3c depicts the windows for extracting smaller signal pieces, with specified step sizes between adjacent windows. Three key features – root mean square (RMS), Wilson amplitude, and zero crossing – were applied to each extracted window to compute the input tensor for the TCN model (Figure 3d). The

equations for these three features are shown in Table S2 (Supporting Information). While the convolutional neural network^[71] excels in detecting spatial relationships within engineering problems such as composite metamaterials,^[72] the TCN model was tailored to capture sequential dependencies and patterns over time, which was composed of multiple residual blocks and a final dense layer^[73] (Figure 3e,f). Each residual block combines a causal convolutional layer, a weight normalization function, a rectified linear unit (ReLU) activation function, and a dropout function. Feature normalization was employed as a common technique to facilitate model convergence and ReLU serves as a simple yet effective activation function in deep learning. The dropout function aids in discarding a portion of the features to prevent overfitting. The causal convolutional layer was characterized by two essential parameters: kernel size (k , number of adjacent elements from the input tensor) and dilation factor (d , the distance between elements used in calculating the output tensor), as indicated in Figure 3g. In a causal convolutional layer, each element of the output tensor was computed by performing a convolutional dot product on a sliding window of $1 + (k-1)*d$ elements of the input tensor. The final dense layer incorporates a softmax activation function, commonly utilized for multiclass classification to output the probability of each class.

2.3. System Design of the Human-Robot Collaboration

An HRC system was designed for assembling and disassembling computer components (Figure 1a). Multiple human operators can collaborate with a single robot manipulator to accomplish the task. The interaction between human operators and robots was realized by the SSI and a hand-tracking interface. The SSI utilized the developed transparent EMG electrode array attached to the facial skin for collecting speech-relevant EMG signals (Figure 1b,c) and the TCN algorithm for decoding EMG signals to speech (detailed in Section 2.2). The collected EMG signals were processed by one TCN model for speaker classification (Figure 1d) and another TCN model for keyword classification (Figure 1e). Once the human operator spoke silently, the speaker classification model first pinpointed the human operator who was issuing commands. Then the keyword classification determined the speech content (i.e., the control commands to guide the robot in performing specific tasks) from the identified human operator. Following signal processing, the identified commands were transmitted to the robot using the MQTT method (Figure 1f).^[74] The robot manipulator responded to the commands by manipulating tools or computer components. The hand-tracking interface (Figure 1g) was enabled by the optical positioning system (elaborated in section 2.4), which assists the robot in assessing the status of the human hand during the interaction process. All processes took place in real time. In the case when multiple human operators were issuing commands through the SSI, the robot manipulator prioritized and executed the earlier command.

2.4. Methods for Interactions between Human Operators and Robots

To enable the robot's execution of manipulation tasks, a Robot Operating System (ROS) was utilized for communication be-

tween the TCN model and the robot manipulator. Once the algorithms recognize the operator and the corresponding command, the system publishes a task command containing this information to a ROS topic. The topic was subscribed to by the robot manipulator in real time. Additionally, several areas were predefined for placing parts and tools, or for recycling. This ensures that upon receiving task commands, the robot manipulator knows where to retrieve parts and tools, or where to place disassembled components.

To facilitate interactions between the robot manipulator and human operators during the hand-over process, a motion capture system, Vicon, was employed to track the hand motion of human operators. This prior research has thoroughly investigated methods for detecting and predicting human arm motions in several manufacturing applications.^[75–78] Multiple reflective markers were attached to the operator's hand (Figure 1g). During the experiment, multiple infrared cameras captured the markers from different angles simultaneously, and then the software reconstructed the movement of the human operator in three dimensions based on the coordinate values. A different ROS topic was utilized to stream the human motion data, allowing the robot to understand where the human hand was. A motion trigger was set when a human operator flipped the hand. This triggering movement can be evidenced by the spatial relationship of markers on both sides of the wrist. Once triggered, the robot will deliver tools or parts to the human operator's hand or take the disassembled components away from the operator.

3. Results and Discussion

3.1. Characterizations of the EMG Electrode Array

The proposed EMG electrode array employs ionic conduction, which offers distinct advantages for biopotential measurements. Ionic conduction facilitates a low interfacial impedance between the electrode and biological systems, promoting the detection of low-amplitude noisy signals and enabling efficient charge injection during stimulation.^[79] The electrode-skin impedance is a key parameter that reflects the electrical properties of the interface and is a crucial indicator of the signal quality.^[80–82] A low electrode-skin impedance indicates good signal transduction from the muscular activities involved in speech to the measurable EMG signals by the electrodes on the skin surface.^[50,83,84] Therefore, low electrode-skin impedance is desirable for high-fidelity tracking of subtle and dynamic speech-relevant EMG signals. Low electrode-skin impedance demands good electrode-skin contact, such that the electrode can follow the rough morphologies of the skin surfaces with minimized gaps.^[85] Previous research has revealed that a low elastic modulus and strong adhesion can improve the contact between the electrode and skin.^[45,86] Based on these requirements, different material compositions for the proposed electrode were evaluated. The conducting layer, serving as the sensing element of the electrode, comprises an ionic liquid and WPU matrix. The ionic liquid was made by dissolving NaCl in quantities close to the maximum solubility in the EG/DI water. Various weight ratios between the ionic liquid and WPU (1:5, 2:5, 3:5) were tested to optimize the electrode.

With an increase in the ratio of ionic liquid, the electrode becomes softer and consistently exhibits non-linear elasticity

(Figure 4a). Notably, the electrode is considerably softer than the human skin's epidermis, which typically possesses an elastic modulus of approximately 1 MPa.^[87] The electrode, as an ionic conductor, has a unique biphasic liquid-solid phase property. The ionic liquid is retained in the interconnected structure of the ionic conductor and changes in solvent content can affect this phase property and, in turn, affect the adhesion.^[88] The electrode with a ratio of 2:5 has a much stronger adhesion than the electrode with a ratio of 1:5 (Figure 4b). Its adhesion force is comparable to that of commercial electrodes, as shown in the referenced study.^[89] The electrode with the 3:5 ratio, however, shows inadequate adhesion force. This can be attributed to the insufficient embedding of the ionic liquid in the WPU matrix, which results in residual ionic liquid on the surface and therefore a reduction in adhesion. In addition, the conductivity (Figure 4c) and Nyquist plot (Figure S4, Supporting Information) show that the conductivity of electrodes increases with increasing the ionic liquid concentration, as a higher concentration yields more ions to establish conductive pathways. All these properties affect the electrode-skin impedance. The electrode with an ionic liquid to WPU of 2:5 exhibits a lower electrode-skin impedance than the other two. The impedance is comparably low compared to the commercial electrode (gold standard) (Figure 4d). Since the electrode array is attached to the facial skin, visually unobtrusiveness is important for wide user acceptance. As shown in Figure 4e, electrodes with different ionic liquid to WPU matrix ratios exhibit similar transmittance across the visible wavelengths. After laminating the PDMS substrate layer, the transmittance slightly decreased, yet maintained a good transmittance of around 80% at most visible wavelengths (Figure 2g; Figure S5, Supporting Information).

Considering the performance above, the weight ratio of 2:5 between ionic liquid and WPU was selected as the final composition for the electrode. Figure S6 (Supporting Information) compares the EMG signals obtained from the developed electrode and a commercial gel electrode placed adjacent. The average Signal-to-Noise Ratio (SNR) for five trials, computed using the equation provided in Table S3 (Supporting Information), was 15.78 dB for the developed electrode and 16.42 dB for the commercial electrode. The comparable SNRs demonstrate that the developed electrode can achieve EMG sensing performance similar to that of the commercial gel electrode. Note the developed electrode is gel-free, stretchable, and transparent, which addresses the limitations of commercial gel electrodes, such as bulkiness, inability to follow skin movements, skin irritation caused by the conductive gel, gel dehydration, and poor user acceptance for facial attachments. The electrode demonstrates robust performance across various conditions. At ambient temperatures between 4 °C and 40 °C, the noise RMS remains within 5 – 7 µV, and the SNR of EMG signals at all temperatures exceeds 15 dB, with only minimal variation (Figure 4f). Relative humidity from 40% to 98% similarly has little impact, leading to noise RMS levels below 7 µV and SNRs at or above 15 dB (Figure S7, Supporting Information). Even during skin stretching and compression, the noise RMS and SNR remain stable, indicating good electrode-skin contact (Figure S8, Supporting Information). However, cable movement introduces significant motion artifacts, raising the noise RMS to above 15 µV (Figure S9, Supporting Information). Applying a high-pass filter can help reduce the noise to around 7 µV, which is slightly higher than that of normal conditions. As illustrated in

Figure S10 (Supporting Information), noise levels and SNRs of EMG signals collected from different pairs of electrodes exhibit similar performance, with minimal sample-to-sample variations. Over five days, noise RMS levels of the electrode show a slight upward trend (Figure S11, Supporting Information) while the SNR of EMG signals on days 4 and 5 is slightly lower than that of the first three days, the SNR values remain high for EMG sensing.

Table S4 (Supporting Information) shows comparisons of existing transparent electrodes in the literature and the electrodes developed in this work for biopotential measurements. These transparent electrodes are categorized into ionically conductive and electrically conductive types. The reported ionic electrodes demonstrate higher transmittance compared to the electrically conductive electrodes. Compared to other ionic electrodes, our electrodes exhibit a lower modulus, which is crucial for wearing comfort and ensuring conformal contact at the skin-electrode interface. This conformal contact enhances the signal-to-noise ratio (SNR) of the electrodes.

3.2. Speech-Relevant Signals Acquired from the EMG Electrode Array

Utilizing the procedure detailed in Section 2.1, we collected EMG signals corresponding to eighteen keywords (Figure 4g) from five individuals. EMG electrodes were affixed in the supralabial and infralabial regions (Figure 2i), which are the optimized sensing locations for speech recognition.^[45] All electrodes placed on the neck were excluded compared to our previous work.^[45] The recognition accuracy was maintained with fewer electrodes due to the improvement in the classification algorithm. The four facial muscles involved are the depressor anguli oris (Channel 1), zygomaticus major (Channel 2), zygomaticus minor (Channel 3), and masseter (Channel 4). As an example, Figure 4g presents a single trial of the EMG signal from Channel 1 for the eighteen keywords and Figure S12 (Supporting Information) shows multiple trials of 4-channel signals corresponding to the command "bottom case". Signals from the same keyword by the same speaker can exhibit considerable variation as shown in Figure S13 (Supporting Information), due to the inability of the speaker to consistently control facial muscles while repeating the same keyword. The complexity of speech signals underscores the need for a deep learning approach to aid in classification. Additionally, the differences in signal patterns for the same keyword across different speakers, such as frequency and signal amplitude, allow for the classification of different speakers using the EMG signals.

3.3. Performance of the Silent Speech Recognition Interface

As shown in Figure 5a, the input tensor for training the TCN model is three-dimensional: (NT×NW, NS, NC×NF), where NT, NW, NS, NC, and NF denote the number of trials, number of words, number of steps, number of channels, and number of features, respectively. NT was set to 50, representing the repetition of each keyword 50 times. Since there are eighteen keywords, NW was set to 18 for a single individual and 90 for five individuals. NS was 24, calculated from one trial signal length of 2 s, window length of 0.16 s, and step size of 0.08 s, as explained in Figure S14 (Supporting Information). NC was equal

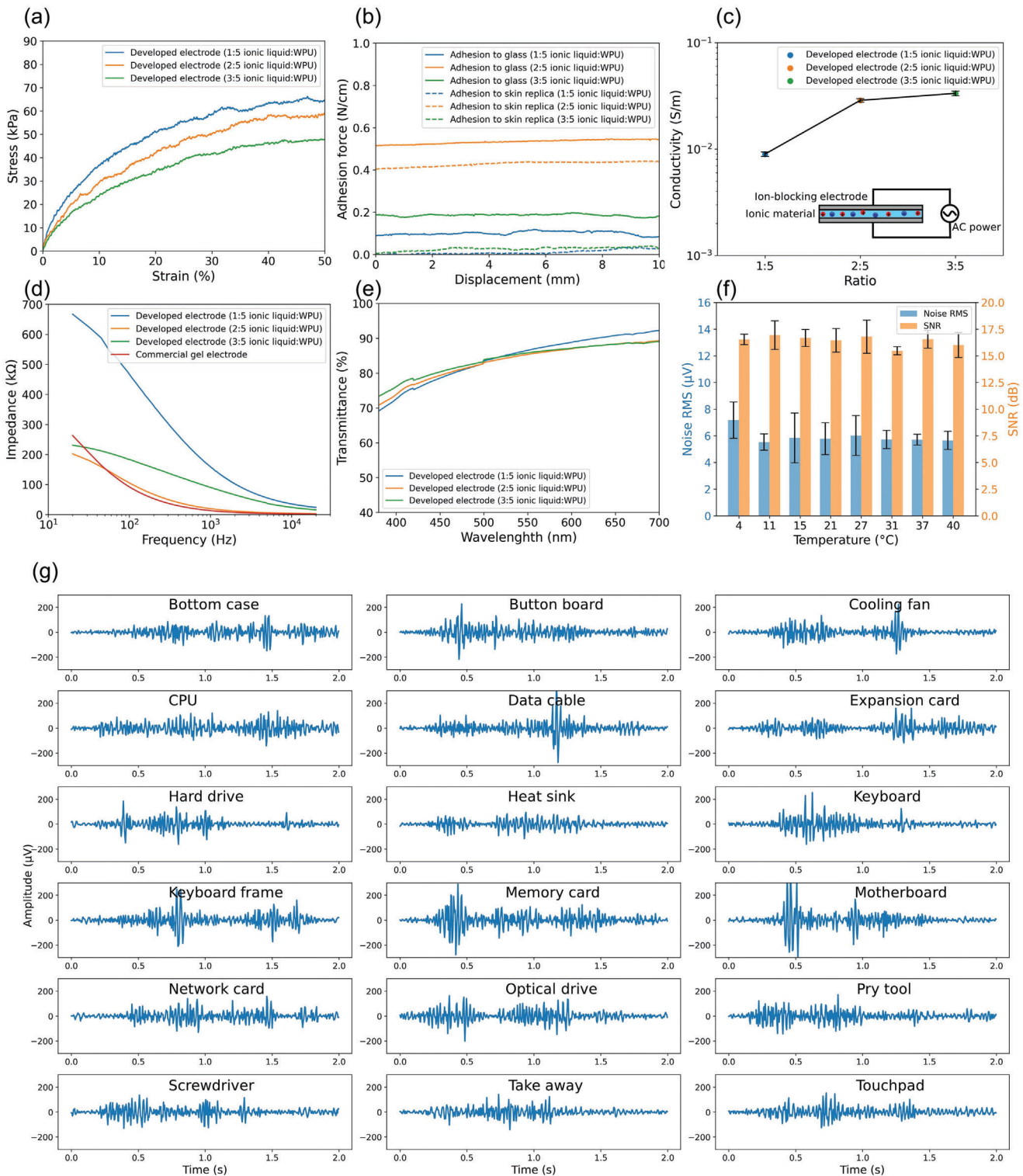


Figure 4. Characterizations of the EMG electrode array. a) Strain-stress curves of the conducting layer of the developed electrode. b) Adhesion of the electrode to the glass and skin replica. c) Conductivity of the ionic conducting layer in the developed electrode array. The conductivity was measured by applying AC signals across the ionic material, which was sandwiched between two ion-blocking electrodes. d) Comparisons of the electrode-skin impedance of the developed electrode and the commercial gel electrode. e) Transmittance of the developed electrode (conducting layer only, other layers are transparent elastomers). f) RMS of noises and SNR of EMG signals acquired at different ambient temperatures. g) The Channel 1 EMG signals of eighteen keywords for HRC. Each piece of the signal is extracted by the data segment program. Only Channel 1 signals are shown as examples.

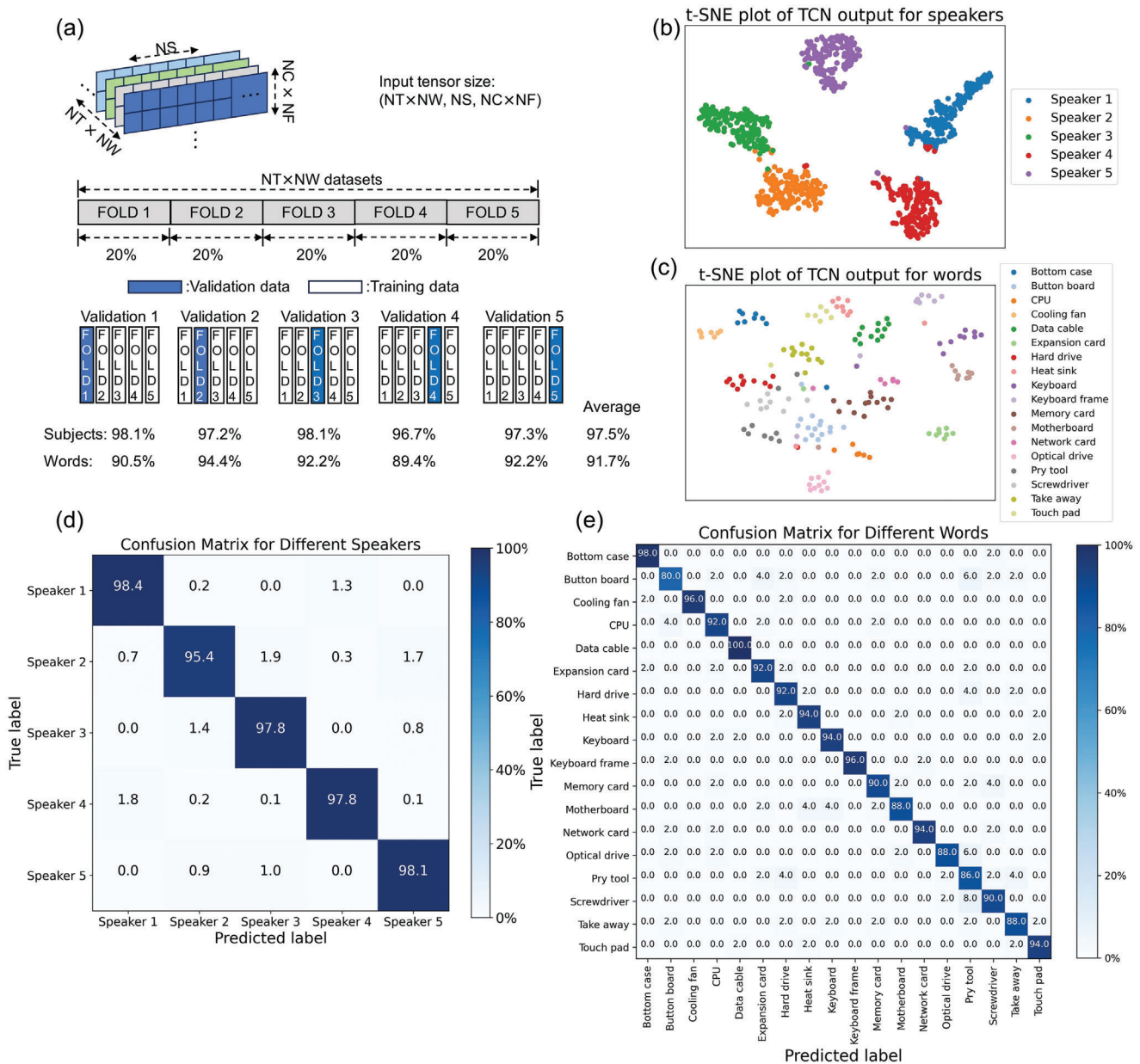


Figure 5. Results for silent speech recognition. a) Input tensor structures and 5-fold validation results. NT, NW, NS, NC, and NF refer to the number of trials, number of keywords, number of steps, number of EMG channels, and number of features, respectively. b) T-distributed stochastic neighbor embedding (t-SNE) of five speakers for the first validation set (as an example). c) t-SNE of eighteen words for the first validation set. d) Confusion matrix for classifying the five speakers. e) Confusion matrix for classifying eighteen words spoken by speaker 1.

to 4 to indicate 4 channels, and NF was 3 due to the use of three features (root mean square, Wilson amplitude, and zero crossing). Hence, the input tensor size for speaker classifications was $(50 \times 90, 24, 4 \times 3)$, while the size for keyword classifications was $(50 \times 18, 24, 4 \times 3)$. The output tensor is one-dimensional, with a size of (50×90) for speaker classification and (50×18) for keyword classification. Five-fold validation was utilized to train the model (Figure 5a). The data was divided into five sets. Four sets were treated as training sets and one set was employed as a testing set each time. Necessary hyperparameter tuning for the TCN model was conducted by using the grid search function. The final

hyperparameters for the TCN model are summarized in Table S5 (Supporting Information).

The speaker classification and keyword classification achieved average accuracies of 97.5% and 91.5%, respectively, despite the use of only four electrodes. Besides, our previous study^[45] has revealed that EMG-based silent speech recognition was not compromised by environmental noises, illustrating the advantage of silent speech interfaces in noisy environments, such as in the manufacturing industry. To visually showcase the high-dimensional features of the TCN model, the t-distributed stochastic neighbor embedding (t-SNE),^[90] which is a well-known

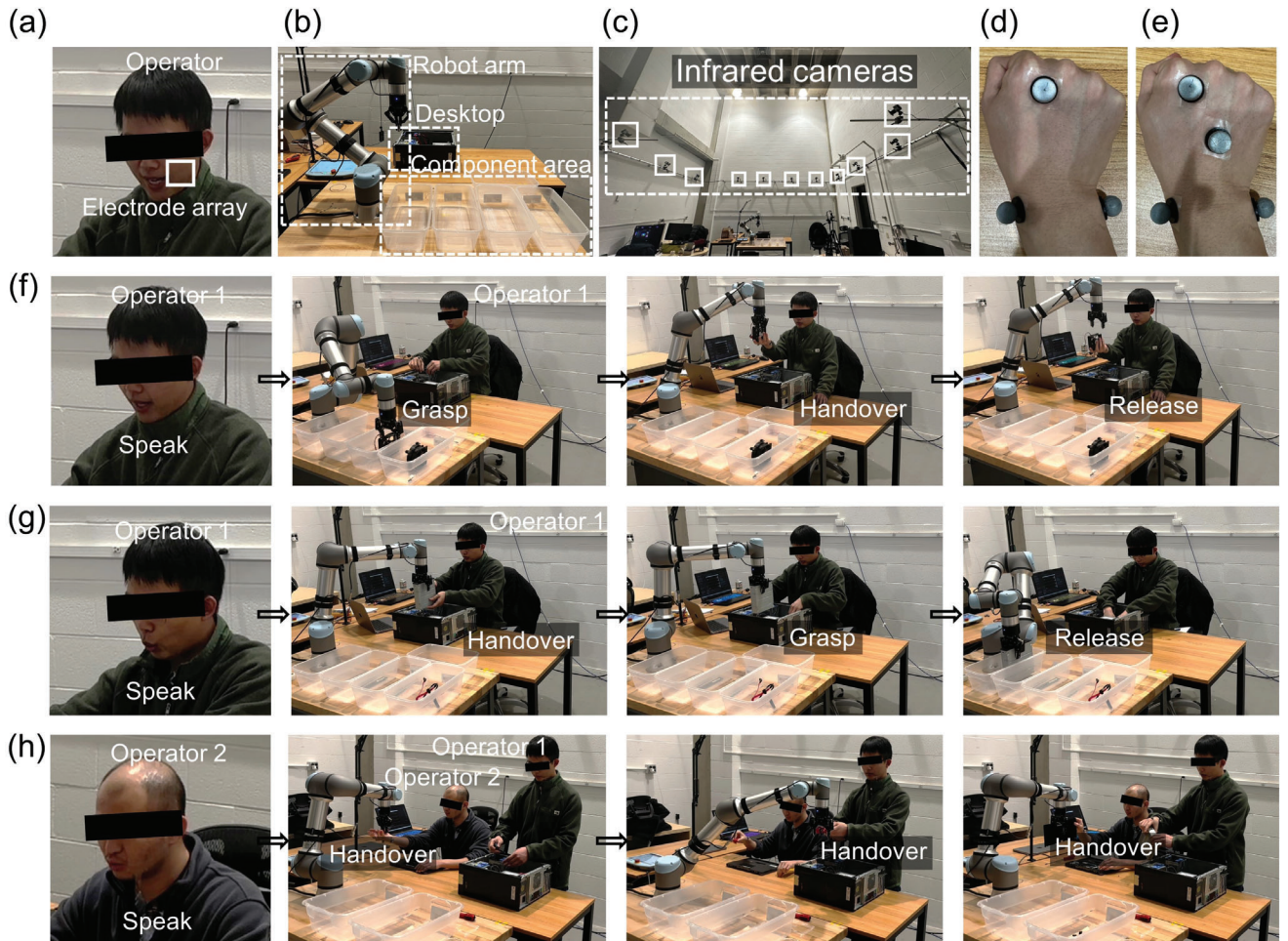


Figure 6. Demonstrations for SSI-assisted HRC. a) A human operator wearing the SSI. b) Experimental setups for the robot manipulator, desktop, and component area. c) The motion capture system based on infrared cameras. d,e) The infrared markers placed on the hand. Video clips showing the collaborative assembly/disassembly processes: f) The assembly process by one human operator and the robot manipulator, g) the disassembly process by one human operator and the robot manipulator, and h) the disassembly process by two human operators and the robot manipulator.

technique to map high-dimensional features in 2D or 3D space, was utilized. The t-SNE plot, based on the output tensor from the final residual block of the TCN model, illustrates the effective grouping of features for different individuals (Figure 5b). Similarly, the t-SNE plot for the keyword classification (Figure 5c) shows that the TCN model can also classify features of each word in a good manner. Figure 5d,e summarize the confusion matrix of the recognition results for different speakers and keywords, respectively. The TCN model performs very well for speaker classification and performs well on most keywords.

3.4. System Performance in Human-Robot Collaboration During Assembly and Disassembly

To demonstrate the application of the developed SSI, we designed an HRC system consisting of SSI and a hand-tracking interface (Figure 6a–e), as detailed in Sections 2.3 and 2.4. Three cases in collaborative manufacturing tasks were demonstrated: A collaborative robot assisting a human operator in both assembly

(Figure 6f) and disassembly (Figure 6g) tasks, as well as a collaborative robot working alongside two human operators in a disassembly task (Figure 6h). With the help of Vicon motion tracking cameras (Figure 6c) and different optical markers placed on the human hands (Figure 6d,e), the robot manipulator can detect the motion trigger when the human operator flips the hand to initiate the hand-over process.

In the one-human-one-robot scenario for assembly, the human operator sat opposite the robotic manipulator, engaging in the assembly of a desktop tower (Figure 6f and Video S1, Supporting Information). The assembly tool (i.e., screwdriver) and desktop components were placed in different predefined areas separately. The human operator issued commands regarding specific tools or components (e.g., expansion card) to the robot manipulator throughout the assembly by making lip movements without producing any sound for each command. After receiving commands from the human operator, the robot manipulator executed the corresponding pick-up task of the requested tool or component. After picking up the tool or component, the manipulator moved it toward the human operator and maintained the grip until the

human operator flipped the hand for the handover process. The tool or component was released by the manipulator and then the human operator picked it up for assembly. In the scenario where one human operator collaborates with one robot for disassembly (Figure 6g and Video S2, Supporting Information), a similar setup to the one-human-one-robot assembly case was adopted. After receiving the command (e.g., data cable) from the human, the robot manipulator retrieved the disassembled part from the human hand and deposited it into the appropriate recycling bin.

As for the two-human-one-robot disassembly case, one human operator was responsible for disassembling the desktop while the other focused on disassembling the laptop. Two separate recycling bins were set up, one for desktop components and one for laptop components (Figure 6h and Video S3, Supporting Information). The robot manipulator first identified the operator using the speaker classification model and then identified the command from the identified operator using the keyword classification model. Under the guidance of the command, the robot manipulator moved toward the operator, detected the motion trigger for the hand-over process, retrieved the component from the hand, and then placed it in the appropriate bin. Our proof-of-concept demonstrations illustrate that the robot manipulator was able to receive instructions from human operators using the developed SSI and execute the corresponding tasks for all three scenarios.

4. Conclusions

In conclusion, this work explores material optimization, structural design, deep learning algorithms, and system integration techniques toward an unobtrusive and effective SSI for HRC. High accuracies, 97.5% for speaker classification and 91.7% for keyword classification, were achieved by the TCN model. Toward the application in HRC for manufacturing, we present a framework for assembly/disassembly tasks by combining the SSI for robot control and the hand-tracking interface for human operator motion detection. Three HRC scenarios, including a collaborative robot assisting a human operator in both assembly and disassembly tasks, and a collaborative robot working alongside two human operators in a disassembly task, were successfully demonstrated. The developed framework for HRC has the potential to improve robot control in noisy environments and to incorporate more human operators, such as individuals with voice disorders, into the manufacturing industry.

Supporting Information

Supporting Information is available from the Wiley Online Library or from the author.

Acknowledgements

This material was based upon work supported by the National Science Foundation under Award No. ECCS-2238363 and ECCS-2335863. S.Y. would like to acknowledge the support from the start-up fund at Stony Brook University. The authors express sincere gratitude to Professor Lifeng Wang and his Ph.D. student Xihang Jiang from the Department of Mechanical Engineering at Stony Brook University for their assistance in tensile

testing. The authors also would like to thank Professor Xinwei Mao and her Postdoctoral Associate Dr. Mian Wang from the Department of Civil Engineering at Stony Brook University for their help with the UV-vis testing system.

Conflict of Interest

The authors declare no conflict of interest.

Data Availability Statement

The data that support the findings of this study are available from the corresponding author upon reasonable request.

Keywords

biopotential electrodes, electromyography, human-robot collaboration, machine learning, silent speech recognition

Received: June 20, 2024

Revised: September 2, 2024

Published online:

- [1] W. Lee, J. J. Seong, B. Ozlu, B. S. Shim, A. Marakhimov, S. Lee, *Sensors* **2021**, 21, 22.
- [2] Y. Lu, H. Tian, J. Cheng, F. Zhu, B. Liu, S. Wei, L. Ji, Z. L. Wang, *Nat. Commun.* **2022**, 13, 1401.
- [3] G. S. Meltzner, J. T. Heaton, Y. Deng, G. De Luca, S. H. Roy, J. C. Kline, *J. Neural. Eng.* **2018**, 15, 046031.
- [4] T. Srivastava, P. Khanna, S. Pan, P. Nguyen, S. Jain, *Proc. ACM Interact. Mob. Wearable Ubiquitous Technol.* **2022**, 6, 140.
- [5] K. Sun, C. Yu, W. Shi, L. Liu, Y. Shi, presented at *Proceedings of the 31st Annual ACM Symposium on User Interface Software and Technology*, ACM, Berlin, Germany **2018**, p. 581.
- [6] Q. Zhang, D. Wang, R. Zhao, Y. Yu, *Proc. ACM Interact. Mob. Wearable Ubiquitous Technol.* **2021**, 5, 43.
- [7] G. Bolano, A. Roennau, R. Dillmann, presented at *27th IEEE International Symposium on Robot and Human Interactive Communication (RO-MAN)*, IEEE, Nanjing, China **2018**, p. 1075.
- [8] G. Bolano, L. Ivani, A. Roennau, R. Dillmann, presented at *2021 30th IEEE International Conference on Robot & Human Interactive Communication (RO-MAN)*, IEEE, Vancouver, Canada **2021**, p. 806.
- [9] J. N. Pires, G. Bugmann, *Ind. Robot* **2005**, 32, 505.
- [10] P. Gustavsson, A. Syberfeldt, R. Brewster, L. Wang, *Proc. CIRP* **2017**, 63, 396.
- [11] J. Tasevski, M. Nikolic, D. Miskovic, *Serb. J. Electr. Eng.* **2013**, 10, 219.
- [12] Y. Li, A. Parsan, B. Wang, P. Dong, S. Yao, R. Qin, *Eng. Appl. Artif. Intell.* **2023**, 117, 105597.
- [13] Y. Sun, W. Wang, Y. Chen, Y. Jia, *IEEE Trans. Syst. Man. Cybern.* **2022**, 52, 728.
- [14] Y. Chen, W. Wang, Z. Abdollahi, Z. Wang, J. Schulte, V. Krovi, Y. Jia, *IEEE Robot. Autom. Mag.* **2018**, 25, 107.
- [15] H. Bley, G. Reinhart, G. Seliger, M. Bernardi, T. Korne, *CIRP Ann.* **2004**, 53, 487.
- [16] M.-L. Lee, X. Liang, B. Hu, G. Onel, S. Behdad, M. Zheng, *J. Manuf. Sci. Eng.* **2024**, 146, 020902.
- [17] W. Wang, R. Li, Y. Chen, Y. Sun, Y. Jia, *IEEE Trans. Autom. Sci. Eng.* **2022**, 19, 2339.
- [18] Z. H. Zhou, G. Y. Zhao, X. P. Hong, M. Pietikainen, *Image Vis. Comput.* **2014**, 32, 590.

- [19] Y. M. Assael, B. Shillingford, S. Whiteson, N. De Freitas, (Preprint) arXiv, arXiv:1611.01599 **2016**.
- [20] A. Fernandez-Lopez, O. Martinez, F. M. Sukno, presented at *Proceedings of the 2017 12th International Conference on Automatic Face and Gesture Recognition*, IEEE, Washington DC, USA **2017**, p. 208.
- [21] T. Afouras, J. S. Chung, A. Senior, O. Vinyals, A. Zisserman, *IEEE Trans. Pattern Anal. Mach. Intell.* **2022**, *44*, 8717.
- [22] B. Denby, M. Stone, in *Proceedings of the 2004 IEEE International Conference on Acoustics, Speech, and Signal Processing*, IEEE, Montreal, Canada **2004**, p. 685.
- [23] A. Jaumard-Hakoun, K. Xu, C. Leboulenger, P. Roussel-Ragot, B. Denby, presented at Proceedings of Interspeech 2016, ISCA, San Francisco, USA **2016**, p. 1467.
- [24] J. Tang, A. LeBel, S. Jain, A. G. Huth, *Nat. Neurosci.* **2023**, *26*, 858.
- [25] G. Wang, Y. Zou, Z. Zhou, K. Wu, L. M. Ni, *IEEE Trans. Mob. Comput.* **2016**, *15*, 2907.
- [26] A. Bedri, H. Sahni, P. Thukral, T. Starner, D. Byrd, P. Presti, G. Reyes, M. Ghovanloo, Z. Guo, *Computer* **2015**, *48*, 54.
- [27] R. Hofe, S. R. Ell, M. J. Fagan, J. M. Gilbert, P. D. Green, R. K. Moore, S. I. Rybchenko, *Speech Commun.* **2013**, *55*, 22.
- [28] J. S. Brumberg, A. Nieto-Castanon, P. R. Kennedy, F. H. Guenther, *Speech Commun.* **2010**, *52*, 367.
- [29] T. Schultz, M. Wand, T. Hueber, D. J. Krusienski, C. Herff, J. S. Brumberg, *IEEE/ACM Trans. Audio Speech Lang. Process.* **2017**, *25*, 2257.
- [30] S. L. Metzger, K. T. Littlejohn, A. B. Silva, D. A. Moses, M. P. Seaton, R. Wang, M. E. Dougherty, J. R. Liu, P. Wu, M. A. Berger, I. Zhuravleva, A. Tu-Chan, K. Ganguly, G. K. Anumanchipalli, E. F. Chang, *Nature* **2023**, *620*, 1037.
- [31] F. R. Willett, E. M. Kunz, C. Fan, D. T. Avansino, G. H. Wilson, E. Y. Choi, F. Kamdar, M. F. Glasser, L. R. Hochberg, S. Druckmann, K. V. Shenoy, J. M. Henderson, *Nature* **2023**, *620*, 1031.
- [32] K. Brigham, B. V. Kumar, presented at *Proceedings of the 2010 4th International Conference on Bioinformatics and Biomedical Engineering*, IEEE, Chengdu, China **2010**, p. 1.
- [33] P. Suppes, Z. L. Lu, B. Han, *Proc. Natl. Acad. Sci. USA* **1997**, *94*, 14965.
- [34] P. Khanna, T. Srivastava, S. Pan, S. Jain, P. Nguyen, presented at *Proceedings of the 22nd International Workshop on Mobile Computing Systems and Applications*, ACM, Virtual, United Kingdom **2021**, p. 44.
- [35] J. Rekimoto, Y. Nishimura, presented at *Proceedings of Augmented Humans Conference 2021*, ACM, Rovaniemi, Finland **2021**, p. 91.
- [36] J. A. Gonzalez, L. A. Cheah, A. M. Gomez, P. D. Green, J. M. Gilbert, S. R. Ell, R. K. Moore, E. Holdsworth, *IEEE/ACM Trans. Audio Speech Lang. Process.* **2017**, *25*, 2362.
- [37] P. W. Schonle, K. Grabe, P. Wenig, J. Hohne, J. Schrader, B. Conrad, *Brain Lang.* **1987**, *31*, 26.
- [38] P. Dong, Y. Li, S. Chen, J. T. Grafstein, I. Khan, S. Yao, *Mater. Horiz.* **2023**, *10*, 5607.
- [39] Y. Jin, Y. Gao, X. Xu, S. Choi, J. Li, F. Liu, Z. Li, Z. Jin, *Proc. ACM Interact. Mob. Wearable Ubiquitous Technol.* **2022**, *6*, 57.
- [40] J. Wang, C. Pan, H. Jin, V. Singh, Y. Jain, J. I. Hong, C. Majidi, S. Kumar, *Proc. ACM Interact. Mob. Wearable Ubiquitous Technol.* **2019**, *3*, 155.
- [41] T. Kim, Y. Shin, K. Kang, K. Kim, G. Kim, Y. Byeon, H. Kim, Y. Gao, J. R. Lee, G. Son, T. Kim, Y. Jun, J. Kim, J. Lee, S. Um, Y. Kwon, B. G. Son, M. Cho, M. Sang, J. Shin, K. Kim, J. Suh, H. Choi, S. Hong, H. Cheng, H. G. Kang, D. Hwang, K. J. Yu, *Nat. Commun.* **2022**, *13*, 5815.
- [42] H. Yoo, E. Kim, J. W. Chung, H. Cho, S. Jeong, H. Kim, D. Jang, H. Kim, J. Yoon, G. H. Lee, H. Kang, J. Y. Kim, Y. Yun, S. Yoon, Y. Hong, *ACS Appl. Mater. Interfaces* **2022**, *14*, 54157.
- [43] Y. H. Wang, T. Y. Tang, Y. Xu, Y. Z. Bai, L. Yin, G. Li, H. M. Zhang, H. C. Liu, Y. A. Huang, *npj Flex. Electron.* **2021**, *5*, 20.
- [44] H. Liu, W. Dong, Y. Li, F. Li, J. Geng, M. Zhu, T. Chen, H. Zhang, L. Sun, C. Lee, *Microsyst. Nanoeng.* **2020**, *6*, 16.
- [45] P. Dong, Y. Song, S. Yu, Z. Zhang, S. K. Mallipattu, P. M. Djuric, S. Yao, *Small* **2023**, *19*, 2205058.
- [46] X. Xu, X. D. Gu, S. Chen, *Int. J. Heat Mass Transf.* **2023**, *202*, 123720.
- [47] X. Xu, X. D. Gu, S. Chen, *Comput. Methods Appl. Mech. Eng.* **2022**, *398*, 115183.
- [48] J. Tian, M. Li, Z. Han, Y. Chen, X. D. Gu, Q. J. Ge, S. Chen, *Comput. Methods Appl. Mech. Eng.* **2022**, *389*, 114394.
- [49] L. Cheng, J. Li, A. Guo, J. Zhang, *npj Flex. Electron.* **2023**, *7*, 39.
- [50] W. Zhou, S. Yao, H. Wang, Q. Du, Y. Ma, Y. Zhu, *ACS Nano* **2020**, *14*, 5798.
- [51] J. A. Fan, W. H. Yeo, Y. Su, Y. Hattori, W. Lee, S. Y. Jung, Y. Zhang, Z. Liu, H. Cheng, L. Falgout, M. Bajema, T. Coleman, D. Gregoire, R. J. Larsen, Y. Huang, J. A. Rogers, *Nat. Commun.* **2014**, *5*, 3266.
- [52] W. Zou, H. Yu, X. Lv, P. Zhou, H. Guo, Y. Zhong, L. Liu, *Adv. Mater. Interfaces* **2022**, *9*, 2201197.
- [53] B. Sun, R. N. McCay, S. Goswami, Y. Xu, C. Zhang, Y. Ling, J. Lin, Z. Yan, *Adv. Mater.* **2018**, *30*, 1804327.
- [54] S. Yoon, Y. J. Kim, Y. R. Lee, N.-E. Lee, Y. Won, S. Gandla, S. Kim, H.-K. Kim, *NPG Asia Mater* **2021**, *7*, 4.
- [55] B. Shin, S. H. Lee, K. Kwon, Y. J. Lee, N. Crispe, S. Y. Ahn, S. Shelly, N. Sundholm, A. Tkaczuk, M. K. Yeo, H. J. Choo, W. H. Yeo, *Adv. Sci.* **2024**, *11*, 2404211.
- [56] K. Lee, X. Ni, J. Y. Lee, H. Arafa, D. J. Pe, S. Xu, R. Avila, M. Irie, J. H. Lee, R. L. Easterlin, D. H. Kim, H. U. Chung, O. O. Olabisi, S. Getaneh, E. Chung, M. Hill, J. Bell, H. Jang, C. Liu, J. B. Park, J. Kim, S. B. Kim, S. Mehta, M. Pharr, A. Tzavelis, J. T. Reeder, I. Huang, Y. Deng, Z. Xie, C. R. Davies, et al., *Nat. Biomed. Eng.* **2020**, *4*, 148.
- [57] L. Zhang, K. S. Kumar, H. He, C. J. Cai, X. He, H. Gao, S. Yue, C. Li, R. C. Seet, H. Ren, J. Ouyang, *Nat. Commun.* **2020**, *11*, 4683.
- [58] H. Sipahi, R. Reis, O. Dinc, T. Kavaz, A. Dimoglo, A. Aydin, *Hum. Exp. Toxicol.* **2019**, *38*, 1314.
- [59] M. Rusdi, Y. Moroi, H. Nakahara, O. Shibata, *Langmuir* **2005**, *21*, 7308.
- [60] H. M. Trimble, *Ind. Eng. Chem.* **1931**, *23*, 165.
- [61] P. Geng, A. Zore, M. R. Van De Mark, *Polymers* **2020**, *12*, 2752.
- [62] X.-F. Wei, E. Linde, M. S. Hedenqvist, *npj Mater. Degrad.* **2019**, *3*, 18.
- [63] C. J. Wang, M. Cai, Z. M. Hao, S. Nie, C. Y. Liu, H. G. Du, J. Wang, W. Q. Chen, J. Z. Song, *Adv. Intell. Syst.* **2021**, *3*, 2100031.
- [64] S. Kabiri Ameri, R. Ho, H. Jang, L. Tao, Y. Wang, L. Wang, D. M. Schnyer, D. Akinwande, N. Lu, *ACS Nano* **2017**, *11*, 7634.
- [65] OpenBCI, Cyton Specs, <https://docs.openbci.com/Cyton/CytonSpecs/>, (accessed: August 2024).
- [66] OpenBCI, Cyton Getting Started Guide <https://docs.openbci.com/GettingStarted/Boards/CytonGS/>, (accessed: August 2024).
- [67] BrainFlow, Python Real Time Plot, <https://brainflow.readthedocs.io/en/stable/Examples.html#python-real-time-plot>, (accessed: August 2024).
- [68] C. E. Shannon, *Proc. IRE* **1949**, *37*, 10.
- [69] NASA, Visible Light, https://science.nasa.gov/ems/09_visiblelight/, (accessed: April 2024).
- [70] Y. Ding, Z. Zheng, *Matter* **2022**, *5*, 2570.
- [71] Y. LeCun, Y. Bengio, G. Hinton, *Nature* **2015**, *521*, 436.
- [72] X. Jiang, F. Liu, L. Wang, *Theor. Appl. Mech. Lett.* **2023**, *13*, 100485.
- [73] C. Lea, M. D. Flynn, R. Vidal, A. Reiter, G. D. Hager, presented at *Proceedings of the IEEE Conference on Computer Vision and Pattern Recognition*, IEEE, Honolulu, USA **2017**, p. 156.
- [74] U. Hunkeler, H. L. Truong, A. Stanford-Clark, presented at *Proceedings of the 2008 3rd International Conference on Communication System Software and Middleware and Workshops*, IEEE, Bangalore, India **2008**, p. 791.
- [75] S. Tian, X. Liang, M. H. Zheng, presented at *2023 American Control Conference*, IEEE, San Diego, USA, **2023**, p. 3356.
- [76] S. Tian, M. Zheng, X. Liang, *IEEE Robot. Autom. Lett.* **2024**, *9*, 6232.

- [77] K. A. Eltouny, W. Liu, S. Tian, M. Zheng, X. Liang, *IEEE Robot. Autom. Lett.* **2024**, 9, 2192.
- [78] X. Zhang, S. Tian, X. Liang, M. Zheng, S. Behdad, *J. Comput. Inf. Sci. Eng.* **2024**, 24, 5.
- [79] D. C. Martin, G. G. Malliaras, *ChemElectroChem* **2016**, 3, 686.
- [80] G. Li, S. Wang, Y. Y. Duan, *Sens. Actuators, B* **2017**, 241, 1244.
- [81] S. S. Yao, Y. Zhu, *Jom* **2016**, 68, 1145.
- [82] S. Yao, J. Yang, F. R. Poblete, X. Hu, Y. Zhu, *ACS Appl. Mater. Interfaces* **2019**, 11, 31028.
- [83] Q. Qin, J. Li, S. Yao, C. Liu, H. Huang, Y. Zhu, *IEEE Access* **2019**, 7, 20789.
- [84] S. Yao, W. Zhou, R. Hinson, P. Dong, S. Wu, J. Ives, X. Hu, H. Huang, Y. Zhu, *Adv. Mater. Technol.* **2022**, 7, 2101637.
- [85] J. W. Jeong, W. H. Yeo, A. Akhtar, J. J. Norton, Y. J. Kwack, S. Li, S. Y. Jung, Y. Su, W. Lee, J. Xia, H. Cheng, Y. Huang, W. S. Choi, T. Bretl, J. A. Rogers, *Adv. Mater.* **2013**, 25, 6839.
- [86] S. D. Wang, M. Li, J. Wu, D. H. Kim, N. S. Lu, Y. W. Su, Z. Kang, Y. G. Huang, J. A. Rogers, *J. Appl. Mech.* **2012**, 79, 031022.
- [87] C. Li, G. Guan, R. Reif, Z. Huang, R. K. Wang, *J. R. Soc. Interface* **2012**, 9, 831.
- [88] X. Fan, S. Liu, Z. Jia, J. J. Koh, J. C. C. Yeo, C. G. Wang, N. E. Surat'man, X. J. Loh, J. Le Bideau, C. He, Z. Li, T. P. Loh, *Chem. Soc. Rev.* **2023**, 52, 2497.
- [89] L. Pan, P. Cai, L. Mei, Y. Cheng, Y. Zeng, M. Wang, T. Wang, Y. Jiang, B. Ji, D. Li, X. Chen, *Adv. Mater.* **2020**, 32, 2003723.
- [90] L. V. D. Maaten, G. Hinton, *J. Mach. Learn. Res.* **2008**, 9, 2579.